

Edge Segregated Polymorphism in 2D Molybdenum Carbide

Xiaoxu Zhao, Weiwei Sun,* Dechao Geng, Wei Fu, Jiadong Dan, Yu Xie, Paul R. C. Kent, Wu Zhou, Stephen J. Pennycook,* and Kian Ping Loh*

Molybdenum carbide (Mo_2C), a class of unterminated MXene, is endowed with rich polymorph chemistry, but the growth conditions of the various polymorphs are not understood. Other than the most commonly observed *T*-phase Mo_2C , little is known about other phases. Here, Mo_2C crystals are successfully grown consisting of mixed polymorphs and polytypes via a diffusion-mediated mechanism, using liquid copper as the diffusion barrier between the elemental precursors of Mo and C. By controlling the thickness of the copper diffusion barrier layer, the crystal growth can be controlled between a highly uniform AA-stacked *T*-phase Mo_2C and a “wedding cake” like Mo_2C crystal with spatially delineated zone in which the *Bernal*-stacked Mo_2C predominate. The atomic structures, as well as the transformations between distinct stackings, are simulated and analyzed using density functional theory (DFT)-based calculations. *Bernal*-stacked Mo_2C has a *d* band closer to the Fermi energy, leading to a promising performance in catalysis as verified in hydrogen evolution reaction (HER).

Mo_2C , a new member of the MXene family, has attracted enormous interest due to its role as a catalyst in the industrial water-gas shift reaction,^[1] methane reforming,^[2,3] CO_2 reduction,^[4] and hydrogen evolution reaction (HER).^[5–7] To improve its catalytic properties, past research efforts have mainly focused on engineering the nanoscale composition and morphology of this material.^[8,9] Phase engineering offers an alternative approach to tune catalytic properties, in which different crystal stacking arrangements are created by the sliding of one atomic layer over the others in a single unit cell (intralayer polymorph), as well as sliding between different unit cells (interlayer polytypes), thereby producing distinct crystals distinguished by different filling or splitting of the nonbonding *d* orbitals of the transition metal.^[10,11] In MoS_2 , for

example, the semiconducting *H* polymorph can be converted to an electron-rich, metallic *T* polymorph by gliding the sulfur atomic planes by an atomic spacing.^[12] However, less attention has been paid toward phase engineering in MXenes. Other than the most commonly observed AA-stacked *1T*-phase Mo_2C , very little is known about the other intralayer or interlayer stacking combinations in Mo_2C .^[13]

The commonly synthesized α - Mo_2C crystal,^[5,13–15] also known as *1T*- Mo_2C , has a unit cell that is composed of two layers of closed-packed Mo observing *ab* stacking order. The sandwiched C layer is formed by carbon atoms occupying the octahedral vacancies created by two layers of Mo planes, analogous to the intralayer stacking registry in *1T*- MoS_2 .^[16] One way of understanding this structure is by exchanging positions of cation and anion in *1T*- Mo_2C and *1T*- MoS_2 . Unlike the weak vdW coupling in MoS_2 ,^[17] the interlayer coupling in Mo_2C is dominated by the Mo–Mo metallic interactions. This means that the ground state stacking arrangement should be significantly lower in energy compared to other phases, giving rise to a high energy barrier to their interconversion.

Here, we successfully grow Mo_2C crystals consisting of mixed polymorphs and polytypes via a diffusion-mediated mechanism by chemical vapor deposition (CVD), using liquid copper as the diffusion barrier between the elemental precursors of Mo and C. Our growth process allows the chemical potential of the elemental precursors to change drastically between the edges and the center regions, leading to distinct phase segregation between the edge and the basal plane. Using atomic-resolution scanning transmission electron microscopy–annular

Dr. X. X. Zhao, Dr. D. C. Geng, Dr. W. Fu, Prof K. P. Loh
Department of Chemistry
National University of Singapore
3 Science Drive 3, Singapore 17543, Singapore
E-mail: chmlohkp@nus.edu.sg


Dr. X. X. Zhao, J. D. Dan, Prof S. J. Pennycook
NUS Graduate School for Integrative Sciences and Engineering
National University of Singapore
13 Centre for Life Sciences, #05-01, 28 Medical Drive, Singapore 117456,
Singapore
E-mail: steve.pennycook@nus.edu.sg

Dr. W. W. Sun, Dr. Y. Xie, Dr. P. R. C. Kent
Center for Nanophase Materials Sciences
Oak Ridge National Laboratory
Oak Ridge, TN 37831, USA
E-mail: sunw@ornl.gov

J. D. Dan, Prof S. J. Pennycook
Department of Materials Science and Engineering
National University of Singapore
9 Engineering Drive 1, Singapore 117575, Singapore

Dr. P. R. C. Kent
Computational Sciences and Engineering Division
Oak Ridge National Laboratory
Oak Ridge, TN 37831, USA

Prof W. Zhou
School of Physical Sciences and CAS Centre for Excellence in Topological
Quantum Computation
University of Chinese Academy of Sciences
Beijing 100049, China

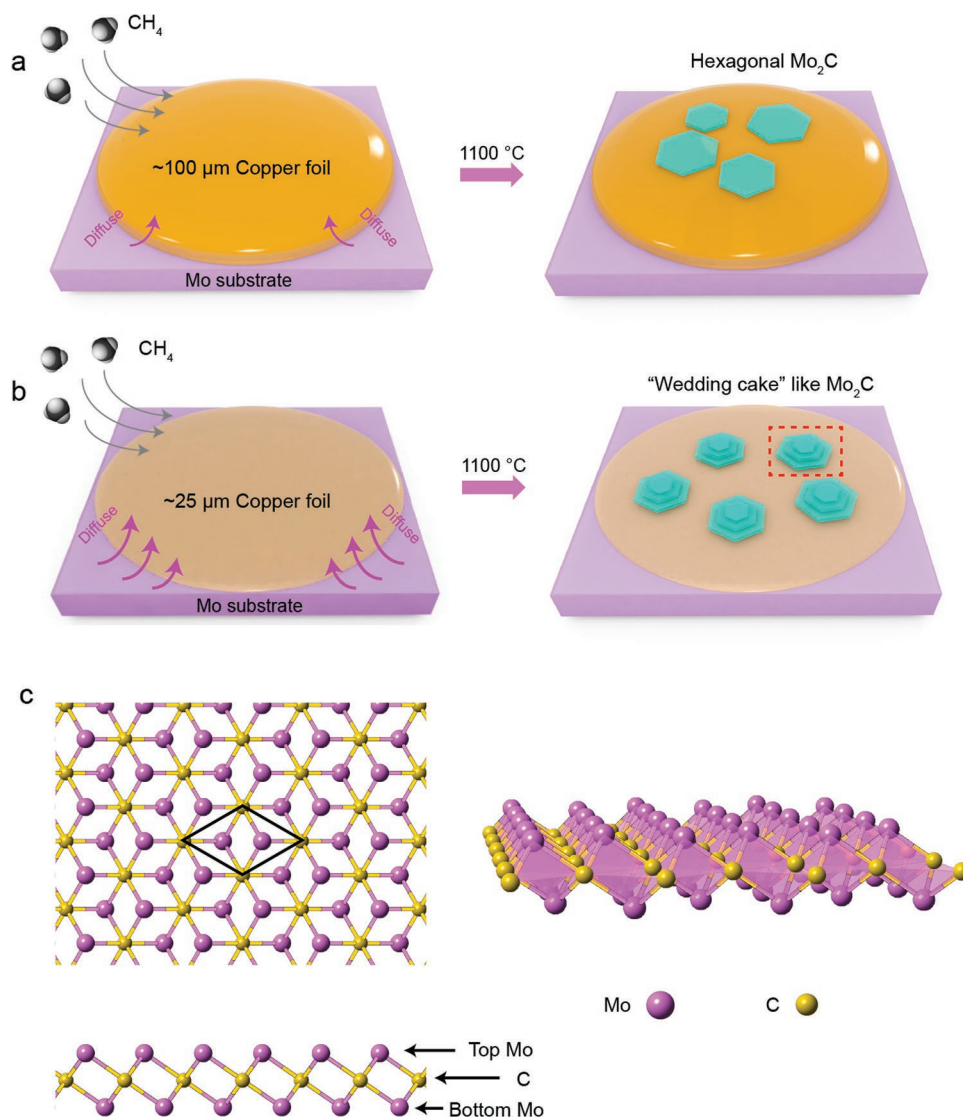
 The ORCID identification number(s) for the author(s) of this article can be found under <https://doi.org/10.1002/adma.201808343>.

DOI: 10.1002/adma.201808343

dark field (STEM-ADF) imaging, a diverse range of polymorphs and stacking polytypes was identified along the edge regions. A full spectrum of intermediate states due to fractional intralayer or interlayer translation, in monolayer and multilayer Mo_2C , was revealed. The atomic structures at various stages of phase transformations were simulated and analyzed by using density functional theory (DFT). All phase transitions observed can be explained by the gliding of the Mo layer along the Mo-Armchair ($\langle 10\bar{1}0 \rangle$) direction, this includes, for example, the $1T\text{-Mo}_2\text{C}$ to $1H\text{-Mo}_2\text{C}$ polymorph transition. Importantly, we found that Mo_2C crystals ring-fenced by Bernal-stacked (AB-stacked) Mo_2C in the edge region show a reduced onset potential for HER compared to conventional AA-stacked crystals.

An ambient pressure CVD system is used for the growth. A Cu foil, which serves as the catalyst as well as a diffusion barrier, is placed on the supporting Mo substrate and introduced into the quartz reactor.^[5,15] At temperatures $> 1100^\circ\text{C}$, the Cu

foil melts and wets the entire Mo substrate. The high reaction temperature results in the formation of a Cu-Mo alloy, through which surface segregation of Mo occurs. The segregated Mo further reacts with the carbon precursor to form Mo_2C crystals. The growth rate of the Mo_2C crystal is mediated by the thickness of the underlying Cu foil due to the variation of Mo diffusion rates. When the Cu foil thickness is reduced from 100 to 25 μm (see the Experimental Section for details), the Mo_2C crystals grow rapidly on the Cu surface and form a “wedding-cake” structure due to the fast diffusion of Mo atoms from the edge to center regions (Scheme 1), as revealed from the optical image (Figure 1a) and atomic force microscope (AFM) (Figure 1b). The height profile shown in the inset of Figure 1b reveals a gradual thickness reduction from the center toward the edge region. Under fast growth conditions, the growth is non-equilibrated leading to a mixture of metastable phases at the edge zone. The atomic structure of the as-grown Mo_2C crystals was



Scheme 1. Schematic illustration showing the controlled growth of a) hexagonal shape single crystals and b) “wedding cake” like Mo_2C crystals by tuning the thickness of the copper diffusion barrier. c) Atomic model of monolayer $1T\text{-phase}$ Mo_2C . The side view and perspective view are depicted in the lower and right panels, respectively.

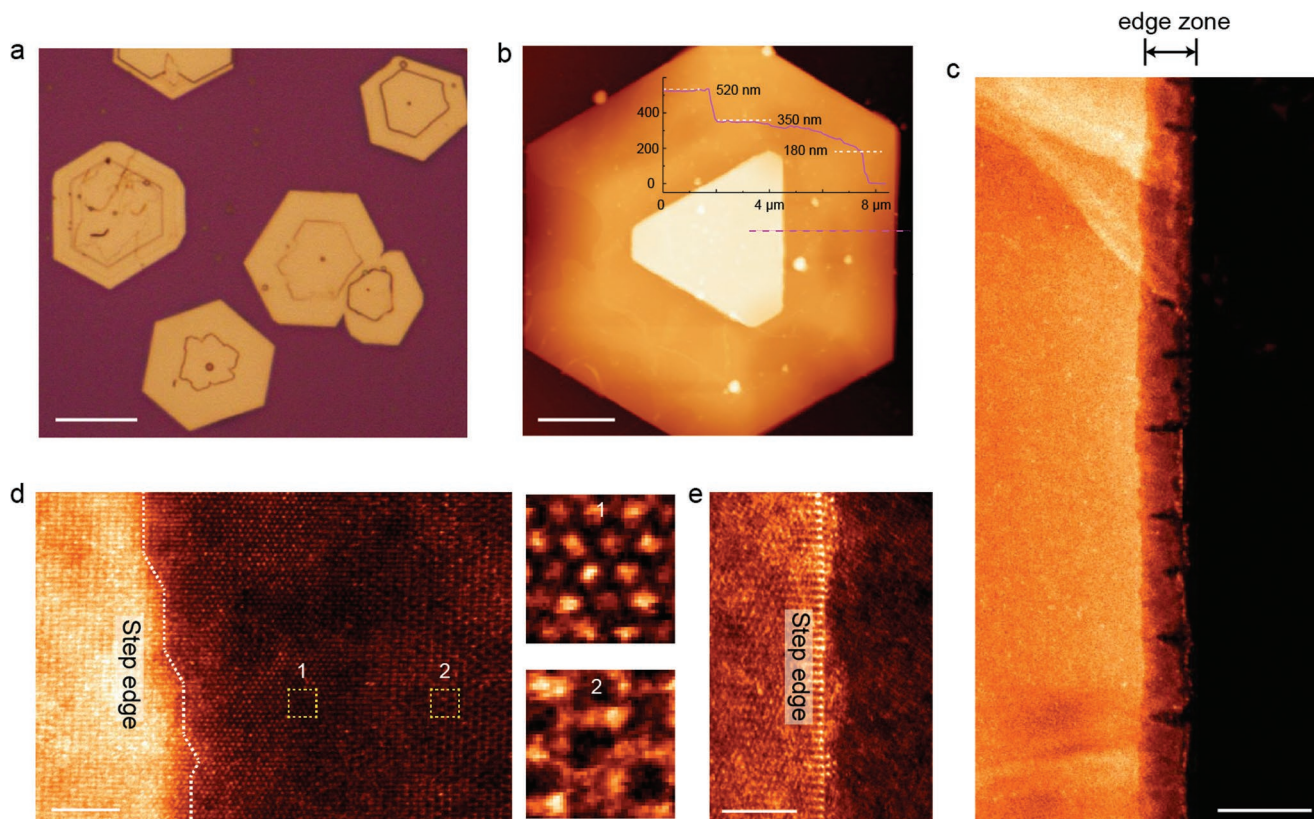


Figure 1. Diffusion-mediated CVD growth of Mo_2C crystals with graded thickness. a) Optical microscope image and b) AFM image showing variation in the thickness of the steps. The inset of (b) reveals the height profile along the red dashed line in the AFM image. c) STEM-ADF image showing delineated edge zones. d) Atomic-resolution STEM-ADF image showing the stacking registry evolution in the vicinity of the step edges. Right panels show atom-resolved stacking registry variations of two different locations; step edges are highlighted by the white dashed lines. e) Atomic structure of the step edge in the edge zone. Scale bars: 10 μm in (a), 4 μm in (b), 200 nm in (c), and 2 nm in (d) and (e).

revealed by atomic-resolution STEM-ADF imaging. Due to the huge atomic number disparity between carbon ($Z = 6$) and molybdenum ($Z = 42$) in Mo_2C , only molybdenum atoms are imaged and carbon atoms are almost invisible in the experimental and simulated STEM-ADF images (Figure S1a, Supporting Information).^[18] The carbon atoms can only be approximately visualized when sufficient coherent elastic scattered electrons are collected (Figure S1b,c, Supporting Information).^[19]

In the wedding cake-like crystal, we observe that metastable polymorphs and polytypes are spatially delineated at the edge zone with a lateral width of ≈ 100 nm. A typical STEM-ADF image showing a well-delineated edge region in a Mo_2C flake is depicted in Figure 1c. The interlayer stacking order reveals a gradual evolution (Figure 1d and Figure S2, Supporting Information) along the edge zone, in which the predominant stacking registry belongs to the *Bernal* type^[20] (region 1 in Figure 1d) and is distinct from the usual AA stacking registry (see the honeycomb structure shown in Figure S1, Supporting Information) in the bulk regions. The presence of a high density of step edges (Figure 1e and Figure S3, Supporting Information) further confirms the crystal growth is mediated by Mo atom diffusion. The fact that this is a diffusion-mediated process is proven by using a ≈ 100 μm thick Cu foil to slow down the diffusion of Mo. In this case, the entire flake is uniform in thickness and the stacking order belongs to the AA type throughout (Figure S4,

Supporting Information).^[14,15] In contrast, the wedding cake-like crystal grown with a 25 μm thick Cu foil presents a gradient of thickness going from monolayer-thick edge to the thicker bulk crystal, this presents a unique opportunity to monitor the evolution in polymorphs and stacking polytypes.

Under the nonequibrated growth conditions where edge zones are richer in Mo than C, various metastable polymorphs attributed to intralayer gliding were observed to coexist in the edge zones of monolayer Mo_2C crystals (Figure 2a and Figure S5, Supporting Information). These polymorphs were induced by the gliding of one Mo atomic plane along the Mo-*Armchair* direction. Due to the in-plane sixfold symmetry in *1T*- Mo_2C , the crystallographic orientation could be classified into two degenerate directions, i.e., Mo-*Armchair* $\langle 10\bar{1}0 \rangle$, and carbon-zigzag (C-ZZ) $\langle 12\bar{1}0 \rangle$ directions, as illustrated in Figure 2b. In monolayer Mo_2C , there are two thermodynamically stable phases, i.e., *1H* and *1T*, where two layers of Mo take *aa* (*1H*) or *ab* (*1T*) stacking orders, respectively^[21]; the prefix “a” or “b” refers to intralayer stacking order in a single unit cell of Mo_2C , while “A” or “B” refers to the interlayer stacking order between two unit cells of Mo_2C ; both phases were observed to be present, as presented in Figure 2c.

To investigate the intralayer gliding behaviors in monolayer Mo_2C crystals, we carried out DFT calculations to investigate the mechanism of phase transitions and map the energy

landscapes driven by the translation of the Mo atomic plane along the Mo-Armchair and C-ZZ directions in the monolayer Mo₂C model. The calculated energy landscape for the gliding of the top Mo layer along the Mo-Armchair direction for one period δ (5.3 Å) is shown in Figure 2d (The same period δ also applies for gliding along the degenerate C-ZZ direction), where insets present atomic models of various intermediate states. Due to the strong Mo-C interactions, the gliding barrier in monolayer Mo₂C is ≈ 200 meV Å⁻², which is almost two times larger than that of the 1H to 1T phase transition in MoS₂.^[22] Besides the common 1T (Figure 2e) and 1H (Figure 2f and Figure S6, Supporting Information) phases located in the saddle points of the energy profiles, another stacking order in which the Mo atomic plane glides for $\frac{1}{6}\delta$, denoted as 1T-ARM_{1/6} (Figure 2g), is commonly seen and marked in the energy landscape. The 1T-ARM_{1/6} stacking order is a metastable state. 1T-ARM_{1/6} (Figure 2g and Figure S7, Supporting Information) is symmetrically distinct from the 1H-phase Mo₂C, and it is composed of periodic single Mo stripes showing an in-plane symmetry

reduction to 2-fold. The experimentally observed 1T-ARM_{1/6} strongly resembles the simulated image derived from the DFT optimized model. On the other hand, the calculated energy barriers for gliding the Mo atomic plane along the C-ZZ direction is larger than that along the Mo-Armchair direction (Figure S8, Supporting Information), and no metastable fractional translated states are found along the entire gliding path. Hence, the simulation results are consistent with the experimental results that all metastable states are likely induced by gliding along the Mo-Armchair direction.

Going from the monolayer edge to bilayer edges and thicker (Figure 3a), we observe stacking polytypes arising from interlayer sliding in bilayer Mo₂C films (Figure 3b). The energy barrier of interlayer sliding (≈ 150 meV Å⁻²) is lower than that of intralayer gliding (≈ 200 meV Å⁻²) as suggested by the DFT (Figure 3c). In a bilayer Mo₂C film, the gliding component is a unit cell of the Mo₂C layer, and the interlayer bonding is described by metallic Mo-Mo interaction. Despite a larger interlayer gliding barrier in bilayer Mo₂C compared to bilayer

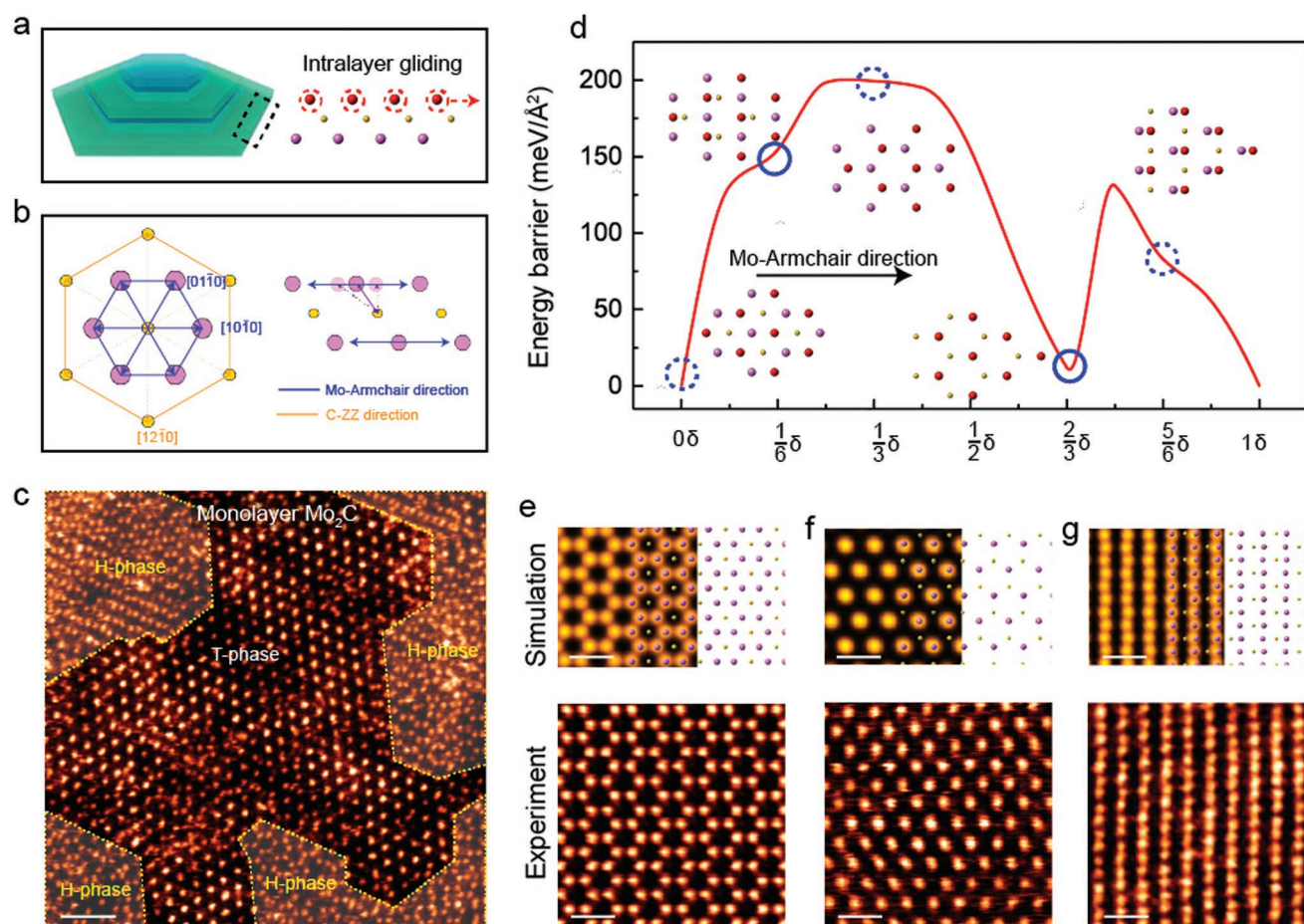


Figure 2. Stacking registry evolution in monolayer Mo₂C. a) Schematic illustration highlighting the sites of intralayer gliding occurring in a wedding cake like Mo₂C crystal. The atomic model depicting the intralayer gliding in a monolayer Mo₂C model is shown on the right. b) Atomic model of 1T-Mo₂C along the [0001] zone axis. The Mo-Armchair and C-ZZ directions are highlighted by blue and yellow false colors, respectively. The side view is depicted in the right panel. c) An atomic-resolution STEM-ADF image showing the coexistence of T- and H-phases in monolayer Mo₂C. d) Energy landscapes for gliding the top Mo atomic plane along the Mo-Armchair direction in monolayer Mo₂C. Insets are atomic models of highlighted stacking registries along the gliding path. e–g) Simulated STEM-ADF images of 1T, 1H, and 1T-ARM_{1/6} stacking registries overlaid with corresponding DFT optimized atomic models. Corresponding experimental STEM-ADF images are depicted in the lower panels. Scale bars: 1 nm in (c) and 0.5 nm in (e)–(g).

graphene^[23] and transition metal dichalcogenides,^[17] various fractional translated stacking orders, induced by a consecutive atomic-scale shift preferentially along the Mo-ZZ direction, were found in the edge zones (Figure S9, Supporting Information), including, e.g., AA-ARM_{1/6} (Figure 3d and Figure S10, Supporting Information), *Bernal* (AA-ARM_{1/3}) (Figure 3e and Figure S11, Supporting Information), and AA-ARM_{1/2} (Figure 3f and Figure S12, Supporting Information), which are induced by interlayer fractional translation for $\frac{1}{6}\delta$ (0.9 Å), $\frac{1}{3}\delta$ (1.8 Å), and $\frac{1}{2}\delta$ (2.7 Å) period, respectively. According to DFT calculations, the *Bernal* (AA-ARM_{1/3}) stacking order is thermodynamically more stable by 15 and 45 meV unit⁻¹, respectively, compared to AA-ARM_{1/6} and AA-ARM_{1/2} stacking order. DFT calculations show that local energy minima can be identified among all the metastable phases. Structurally, *Bernal*-stacked Mo₂C reveals a similar interlayer structure with commonly encountered bilayer 3R-stacked MoS₂ or AB-stacked bilayer graphene,^[24,25] and is noncentrosymmetric.^[17]

Further away from the bilayer edges, we observed that Mo₂C crystals undergo interlayer gliding in thicker regions and spotted a large amount of *Bernal* like stacking orders. In multilayer crystals, *Bernal* like Mo₂C can be confirmed by the presence of additional atom blobs (highlighted by pink) in each honeycomb (Figure 4a,b). The additional atom blobs could be induced by Mo atomic plane gliding (intralayer) and/or Mo₂C plane gliding (interlayer). The STEM-ADF image is incoherent and the contrast is varying approximately as $Z^{1.6-1.7}$,^[18] where Z is the atomic number. Therefore, the ratio between the translated Mo layers versus the static Mo layers can be calculated by measuring the intensity ratio between the additional atom blobs (site c) and the atom blobs in the honeycomb (site a or b). Four different regions revealing different degrees of gliding (Figure 4a), along with their simulated images (Figure 4b) derived from “abc,” “abc_{0.75},” “abc_{0.5},” and “abc_{0.25}” stacking orders, are depicted in the lower panels. The atomic model showing the deficiency at the “c” atom sites is depicted

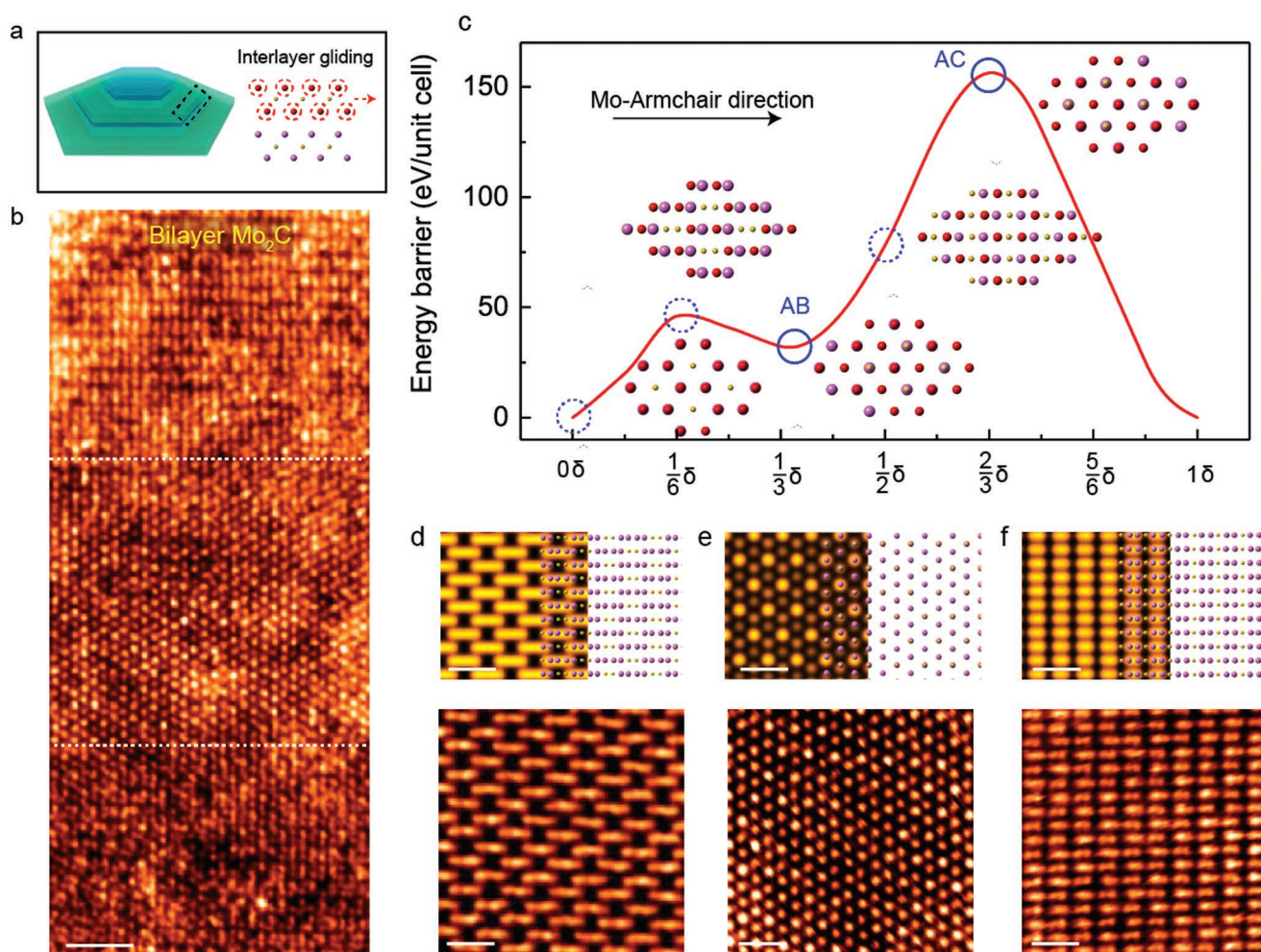


Figure 3. Stacking registry evolution in bilayer Mo₂C. a) Schematic illustration highlighting the sites of interlayer gliding occurring in a wedding cake like Mo₂C crystal. The atomic model depicting the interlayer gliding in a bilayer Mo₂C model is depicted in the right. b) An atomic-resolution STEM-ADF image showing the coexistence of various stacking polytypes as depicted in (d)–(f) bilayer regions. c) Energy landscape for gliding the top Mo₂C layer along the Mo-Armchair direction in bilayer Mo₂C. Insets are atomic models of highlighted stacking registries along the gliding path. Simulated STEM-ADF images of d) AA-ARM_{1/6}, e) *Bernal* (AA-ARM_{1/3}), and f) AA-ARM_{1/2} stacking registries overlaid with the corresponding DFT optimized atomic models. Corresponding experimental STEM-ADF images are depicted in the lower panels. Scale bars: 1 nm in (b) and 0.5 nm in (d)–(f).

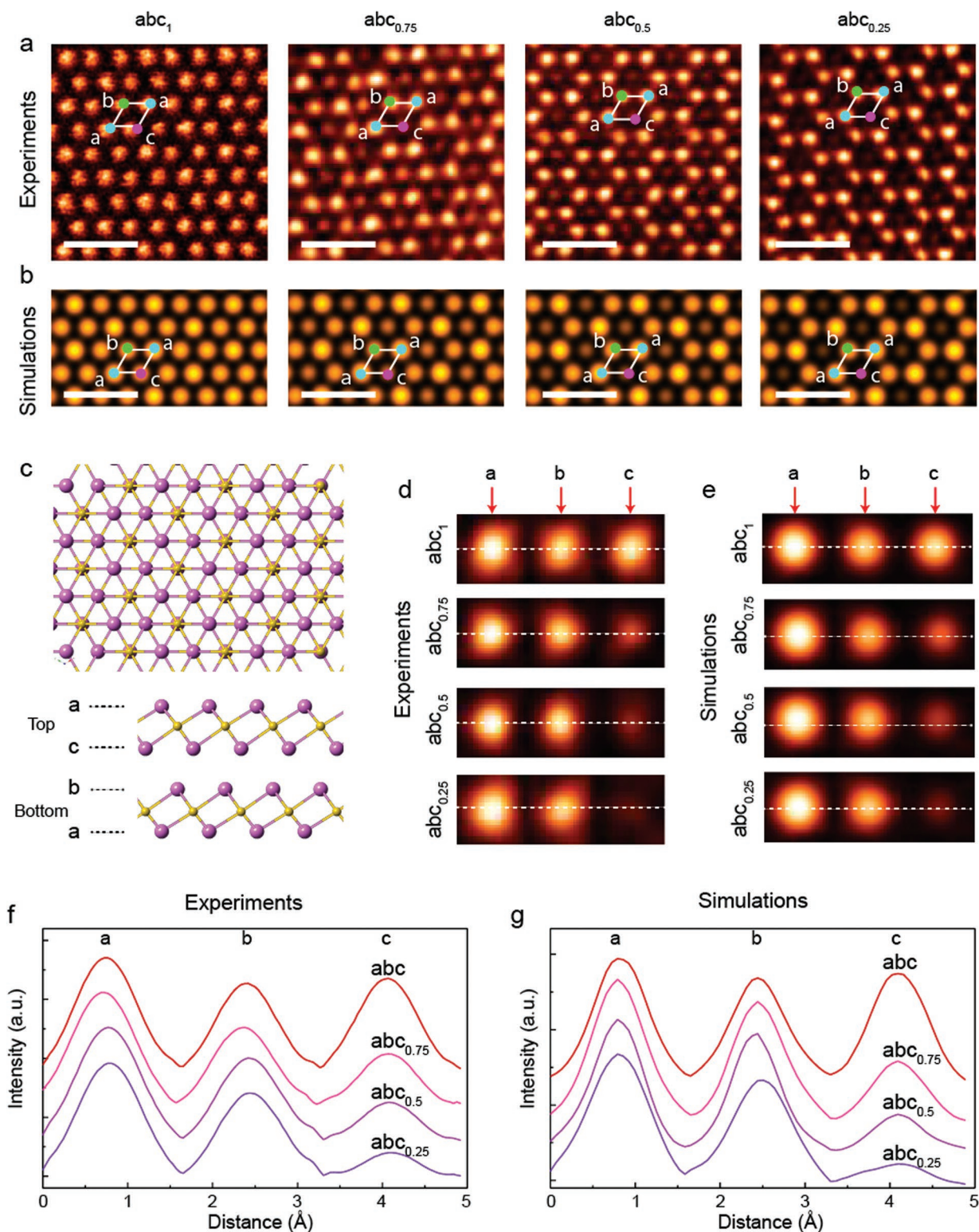


Figure 4. Electron microscopy study of the *Bernal* (abc_x , $x = 0.25$ to 1) stacking registry in multilayer Mo_2C . a) Atomic resolution STEM-ADF images showing different degrees of gliding in few-layer Mo_2C crystals. The gliding ratio x is defined by calculating the intensity ratio between the static Mo layer versus the gliding Mo layer. b) Corresponding simulated images of *Bernal*-stacked few layer Mo_2C when the gliding ratio $x = 1, 0.75, 0.5$, and 0.25 , respectively. Three atomic sites, a, b, and c, representing the density of a, b, and c components, respectively, in the unit cell are highlighted in (a) and (b). c) Atomic model of the *Bernal*-stacked Mo_2C and the side view showing different layers of a, b, and c components. Averaged intensity of all atomic sites from d) experimental and e) simulated abc_x ($x = 1, 0.75, 0.5, 0.25$) images. Intensity line profiles of the averaged three representative atomic sites (a, b, and c) in f) experimental and g) simulation results. Scale bars: 0.5 nm .

in Figure 4c. To quantify the intensity ratio between different atom blobs, we integrate the intensity of all equivalent atom sites (Figure 4d,e) in the experimental images (see Methods) in order to reduce the local intensity fluctuations as the probability of forming a defect is equivalent at all atomic positions. The analysed intensity line profiles (Figure 4f,g) agree well with the simulation results, confirming different degrees of gliding in thick regions. Other structures induced by fractional translations are depicted in Figure S13, Supporting Information.

The activation barrier for Mo plane gliding can be reduced by the presence of vacancies. Point defects are abundant in the $1T/1H$ phase boundary (Figure S14, Supporting Information) in monolayer and few layer films (Figure S15, Supporting Information). To understand the role of point defects in the formation of various intermediate states, we employed DFT and constructed a $1T/1H$ lateral phase boundary in monolayer Mo_2C nanoribbon as depicted in Figure S16 (Supporting Information). When the phase boundary contains diverse point defects, i.e., a Mo vacancy and Mo and C divacancy, they stabilize the formation of intermediate states. Hence, the presence of imperfections facilitate the formation of different phases as observed by STEM, which opens a door to manipulating the structures of MXenes and metallic 2D materials via defect engineering.

We now elucidate the stacking dependent properties of the *Bernal*-stacking polytype and compare with that of *AA*-stacked T phase Mo_2C . The various stacking configurations and their energies are displayed in Figure S17 (Supporting Information). The bilayer *Bernal* stacking consists of an *abac* stacking sequence for four Mo atomic layers as opposed to the *abab* stacking sequence in *AA* stacking order. The density of states (DOS) shown in Figure 5a,b clearly indicates that both *AA* and *Bernal* stacked polytypes are metallic with Mo bands dominating the Fermi energy ϵ_f . In the orbital resolved DOS of *AA*-stacked Mo_2C in Figure 5a, the DOS near ϵ_f is mainly due to the Mo-4d states. Between -4.8 and -7 eV, C-2p derived states hybridize with Mo states, and the valence band is dominated by the Mo(4d)-C(2p) hybridization. The upper and lower Mo_2C layers in the *AA* stacking are similar because of the absence of gliding. ϵ_f is situated in a pseudogap, similar to bulk metal carbides and MXenes.^[26,27] In the case of the *Bernal*-stacked Mo_2C , gliding introduces stronger Mo(4d)-C(2p) hybridization in the DOS for both Mo atomic layers, and in fact the lower Mo_2C layer is also perturbed due to the interlayer coupling. Furthermore, the pseudogap that was visible at about -5 eV in the *AA*-stacked Mo_2C is eliminated in *Bernal* stacking and replaced by the tail states due to Mo(4d)-C(2p) hybridization. Around ϵ_f , the two-peak DOS in the *AA* stacking order has been modified and transformed to a multiple split-peak feature. Lastly, the electron localization function (ELF) (Figure 5c) and the line profile of the ELF (Figure S18, Supporting Information) indicates that *Bernal* stacked Mo_2C exhibits stronger covalent bonding than the *AA* stacked counterpart, suggesting the gliding has induced partial ionic-covalent transformation.

The linear Brønsted–Evans–Polanyi relation and Hammer–Nørskov d-band models^[28,29] for metals have been widely applied to rationalize activity trends in metal surface-catalyzed reactions. This “golden rule” is usually invoked to explain catalytic activity in multiple systems, including the Pt-WC(0001) surface^[30] and Pt alloys.^[31,32] The distance of the d band

center to $\epsilon_f(\epsilon_d - \epsilon_{bc})$ reflects the activity for charge exchange. With the aid of the linearization energy resolved in the FP-LMTO method, the 4d band center of each Mo layer shown in Figure 5d can be quantitatively characterized. The $\epsilon_d - \epsilon_{bc}$ of the surface Mo layer in *Bernal* stacked Mo_2C is smaller than that in the *AA*-stacked Mo_2C . Moreover, the electron cloud of the surface Mo is more spread out and denser than that of *AA* stacked Mo_2C , suggesting that the former may have greater surface catalytic activity. Prompted by these predictions, we have tested the catalytic activity of wedding-cake crystals containing the *Bernal*-stacked Mo_2C versus that of *AA*-stacked Mo_2C in HER. From the linear sweep voltammograms (LSV, Figure 5e), it is seen that the wedding cake like Mo_2C crystal has a lower onset overpotential (280 meV at 10 mA cm^{-2}) and smaller Tafel slope (75 mV dec^{-1}) as compared to single-crystal Mo_2C (onset potential is 340 meV at 10 mA cm^{-2} and Tafel slope is 82 mV dec^{-1}) (Figure S21, Supporting Information). As an electrocatalyst, *Bernal*-stacked Mo_2C is highly stable and there is almost no discernible decay in the HER current after 1000 cycles (dashed curve in Figure 5e). In addition, the hydrogen adsorption Gibbs free energy (ΔG_{H^*}) of *AA*- and *Bernal*-stacked Mo_2C , an indicator for the HER performance, was calculated. According to the calculations (Figure S22, Supporting Information), *Bernal* stacked Mo_2C has a $\Delta G_{\text{H}^*}^0$ of -0.58 eV as compared to -0.62 eV for *AA*-stacked Mo_2C . An optimal value of $\Delta G \equiv 0$ is obtained when the adsorption and desorption of H^* has low energy barriers, thus *Bernal*-stacked Mo_2C has a lower onset potential for HER.

Our studies show that the use of melted copper as a diffusion barrier between the two elemental precursors (Mo and C) allows CVD growth to be operated under diffusion-limited, nonequilibrium conditions, whereby metastable polymorphs and polytypes can be generated at the edge zones of the crystals, thus affording a strategy to tune the electronic and catalytic properties of the crystals. Under nonequilibrium, fast growth conditions, metastable polymorphs (intraunit cell), and polytypes (interunit cell) dominate the edge regions in which *Bernal* (*AB*) stacking is abundant. All phase transitions observed can be explained by the gliding of the Mo layer along the Mo-*Armchair* $\langle 10\bar{1}0 \rangle$ direction, which are promoted by the presence of Mo vacancies. According to DFT calculations, the *Bernal* stacking order have their d bands closer to the Fermi energy than the *AA* stacked counterpart, thus affording enhanced catalytic reactivity observed in HER. The growth method demonstrated here allow metastable phases to be segregated at the edges of the crystal, which constitute as a new strategy for spatially segregated phase engineering; it can also be applied to other members of the MXene family and to other non-vdW 2D materials, thereby expanding the synthetic space for a wide class of polymorphs and polytypes.

Experimental Section

CVD Grown Mo_2C crystals: The detailed growth method can be seen in the previous report.^[13] Briefly, Cu foil was cut into 10×10 mm² pieces and placed onto a piece of Mo foil. The thickness of the Cu foil for growing wedding cake-like Mo_2C was ≈ 25 μm , and 100 μm thick Cu foil was used for growing uniformly thick Mo_2C crystals. The Cu-on-Mo foils together were loaded into the quartz tube with an outer diameter of 25 mm, inner diameter of 22 mm, and a length of 1220 mm. The

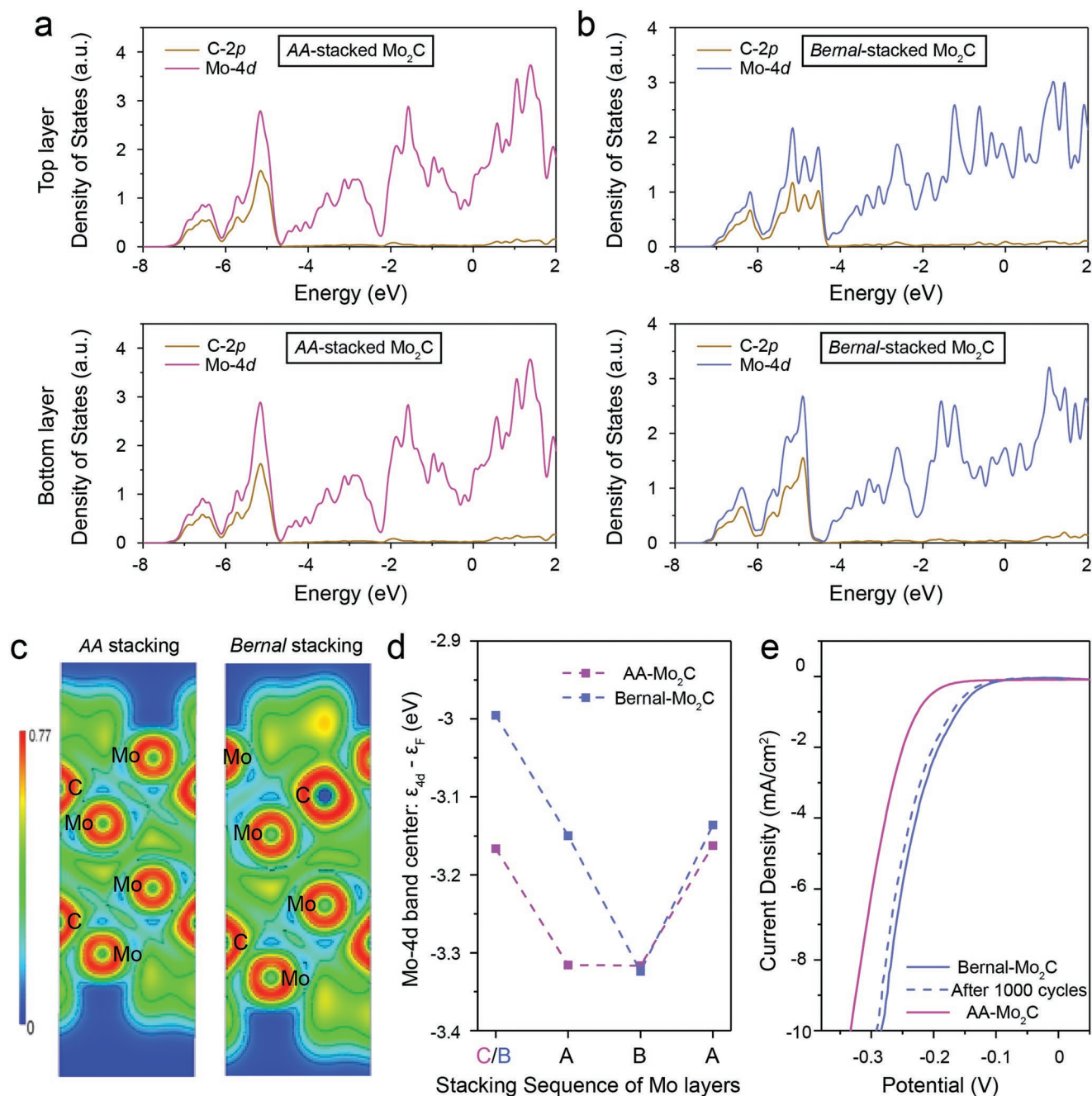


Figure 5. Electronic structure and chemical bonding analysis of AA and *Bernal* stacked polytypes. The atom and orbital projected DOS of upper and lower layers in a) AA-stacked Mo_2C and b) *Bernal*-stacked Mo_2C . The pink and brown curves present DOS of Mo-4d and C-2p orbitals in AA-stacked Mo_2C . The blue and brown curves present DOS of Mo-4d and C-2p orbitals in *Bernal*-stacked Mo_2C . c) The side view of electronic localization function (ELF) of the AA and *Bernal*-stacked Mo_2C with a color bar representing the degree of localization of electrons. d) the distance of the 4d-band center ($\epsilon_{4d} - \epsilon_F$) with respect to ϵ_F of each Mo layer. The pink and blue curves stand for the AA and *Bernal* stacking orders, respectively. e) First linear sweep voltammograms (LSV) scan (blue curve) and the LSV after 1000 cycles (blue dashed curve) for *Bernal*-stacked Mo_2C crystals, and LSV curve (pink curve) of AA-stacked Mo_2C crystals.

substrate was heated to 1100 °C in a horizontal tube furnace under a constant flow of 200 sccm of H_2 gas. Subsequently, 0.6 sccm of CH_4 gas was introduced to the quartz tube at ambient pressure. The growth time was about 3 h. When the growth was complete, the Cu foil together with the Mo foil was quickly unloaded to ensure rapid cooling.

Mo_2C Crystals Sample Transfer: A bubbling assisted transfer method^[33] was employed for transferring Mo_2C crystals grown on the

Mo foil. First ≈ 50 nm poly(methyl methacrylate) (PMMA) (495 kDa molecular weight, 3 wt% in ethyl lactate) was spin coated (2000 r.p.m. for 2 min) onto the Mo foil. was subsequently cured at 170 °C for 5 min. The current density and the corresponding electrolytic voltage were set at ≈ 0.5 A cm^{-2} and ≈ 10 V, respectively. Normally 5 min bubbling time is sufficient to detach the PMMA/ Mo_2C film from the Cu surface. After detaching, the PMMA/ Mo_2C film was placed onto TEM grids with

additional 10 min heating (100 °C) to enhance the binding between the Mo₂C crystals with TEM grids. Next, PMMA/Mo₂C/TEM grids were immersed in hot acetone (60 °C) for ≈2 h to dissolve the PMMA residues. Finally, the Mo₂C/TEM grids were rinsed in isopropyl alcohol (IPA) and acetone for a few times to remove all possible residues.

STEM-ADF Imaging, Processing, and Simulation: STEM-ADF imaging was performed on an aberration-corrected JEOL ARM-200F equipped with a cold field emission gun and ASCOR probe corrector. 80 kV was employed for analyzing edge regions to reduce beam damage, and 200 kV was applied for the interior bulk regions. The convergence semiangle of the probe was set as ≈30 mrad. ADF images were collected for a half-angle ranging from ≈68 to 280 mrad. The dwell time was fixed at 19 μs pixel⁻¹. STEM-ADF image processing was first convoluted by a series of Laplacian of Gaussians (LoG) filteres, the positions of atomic columns were located by finding the local maxima of the filtered series. Subsequently, the intensity extracted from the same type of atom blobs were integrated and normalized to obtain a relatively smoothed 2D point-spread function, which is used for quantitative image comparison. Image simulations were performed using the QSTEM package with a probe size of ≈1 Å. Image intensity processing was carried out using Python scripts.

HER Sample Preparation and Measurement: The as-grown Mo₂C crystals were transferred onto a 3 mm diameter glassy carbon (GC) electrode using the bubbling assisted transfer method. The GC plate was polished by diamond slurries prior to transfer. All electrochemical measurements were done under ambient conditions using a three-electrode cell. Standard Ag/AgCl electrodes and a Pt foil were used as the reference and counter electrode, respectively. The LSV was recorded in 0.5 M H₂SO₄ electrolyte with a scan rate of 2 mV s⁻¹ on an Autolab 302 N electrochemical workstation. The LSV curves were averaged over three different samples.

DFT Calculations: To derive structures and energies of various stacked Mo₂C, DFT calculations were carried out within the Vienna Ab-initio Simulation Package (VASP).^[34–36] On the basis of the projector augmented-wave (PAW)^[37,38] method, the generalized gradient approximation (GGA) of Perdew, Burke, and Ernzerhof (PBE)^[39] was adopted. Within PAW, the 4d and 5s states were considered as the valence states for Mo with frozen semicore states of 4s and 4p. The 2s and 2p states were treated as the valence states for C. A cut-off energy of 580 eV was used in all calculations, and for Brillouin zone (BZ) integration a 15*15*1 Monkhorst-Pack k-point mesh in the first order Methfessel-Paxton of smearing method^[40] with a width of 0.05 eV was applied. The geometry optimization was stopped once the forces on each atom were less than 10⁻² eV, and the convergence criteria of total energy were set to be 10⁻⁶ eV. Note that for all electronic structure calculations, a dense 19*19*1 Monkhorst-Pack scheme was used for sampling the BZ. In order to investigate the chemical bonding between the different Mo–C bonding types, we have carried out crystal orbital overlapping population (COOP) calculations using the LOBSTER code.^[41,42]

To evaluate the dynamical stability of the newly discovered stacking, we employed the frozen phonon approach implemented in PHONONPY.^[43] The electrical conductivity $\sigma(\mu, T)$ was calculated by using the BoltzWann program.^[44] The relaxation time was set to a constant value of 5.52 fs.^[45] A dense mesh 20 × 20 × 20 for band interpolation and a small energy bin width of 10⁻³ eV were adopted in these calculations. Scalar relativistic electronic structure calculations were performed by using the full-potential linearized muffin-tin orbitals (FP-LMTO) code RSPT.^[46] The muffin-tin spheres, which in a full-potential code are used to divide the physical space in the unit cell, were carefully optimized to offer a good description of the electron density. The valence electrons were described with 5s, 5p, and 4d states for Mo and 2s and 2p states for C. For the basis function in the muffin-tin spheres, where the partial wave $\phi_l(\epsilon, r)$ in is written as $\phi_l(\epsilon_v, r) + (\epsilon - \epsilon_v)\phi_l(\epsilon_v, r)$ at an energy of ϵ_v to find a good trial wave function. Note ϕ_l and ϕ_1 are energy ϵ and position r dependent partial wave function and its derivative. In the framework of RSPT, the position of linearization energy is set to the band center $\left\{ \epsilon_v - \frac{W(k, \phi)}{W(k, \phi)} \right\}$ of each atomic type, energy set as well as orbital l , where W is the Wronskian at the muffin-tin radius. The self-consistent cycles minimize the total energy with to respect linearization energy, and this is clearly always

justifiable since the native feature of self-consistent-field scheme in DFT is to minimize the total energy.

Supporting Information

Supporting Information is available from the Wiley Online Library or from the author.

Acknowledgements

X.Z. and W.S. contributed equally to this work. K.P.L thanks MOE Tier 2 grant “Porous, Conjugated Molecular Framework for Energy Storage” (MOE2016-T2-1-003), National Research Foundation, Prime Minister’s Office. W.Z. acknowledges support from the National Key R&D Program of China (2018YFA0305800) and the Natural Science Foundation of China (51622211). S.J.P. thanks the National University of Singapore for funding and MOE for a Tier 2 grant “Atomic scale understanding and optimization of defects in 2D materials” (MOE2017-T2-2-139). Theoretical calculations (W.S., Y.X., and P.K.) were supported as part of the Fluid Interface Reactions, Structures and Transport (FIRST) Center, an Energy Frontier Research Center funded by the U.S. Department of Energy, Office of Science, Office of Basic Energy Sciences. This research used resources of the National Energy Research Scientific Computing Center, a DOE Office of Science User Facility supported by the Office of Science of the U.S. Department of Energy under Contract No. DE-AC02-05CH11231. W.S. acknowledges Dr. Igor Di Marco at Uppsala University to provide the latest version of relativistic spin polarized toolkit (RSPT), an FP-LMTO code, and the computational resources at the National Supercomputing Center in Sweden with project ID SNIC2017-1-374. This manuscript was coauthored by UT-Battelle, LLC, under contract DE-AC05-00OR22725 with the U.S. Department of Energy (DOE). The publisher, by accepting the article for publication, acknowledges that the U.S. government retains a nonexclusive, paid-up, irrevocable, worldwide license to publish or reproduce the published form of this manuscript or allow others to do so for U.S. government purposes. DOE will provide public access to these results of federally sponsored research in accordance with the DOE Public Access Plan (<http://energy.gov/downloads/doe-public-access-plan>).

Conflict of Interest

The authors declare no conflict of interest.

Keywords

molybdenum carbide, MXene, phase engineering, scanning transmission electron microscopy

Received: December 27, 2018

Revised: February 3, 2019

Published online:

- [1] S. Yao, X. Zhang, W. Zhou, R. Gao, W. Xu, Y. Ye, L. Lin, X. Wen, P. Liu, B. Chen, E. Crumlin, J. Guo, Z. Zuo, W. Li, J. Xie, L. Lu, C. J. Kiely, L. Gu, C. Shi, J. A. Rodriguez, D. Ma, *Science* **2017**, 357, 389.
- [2] S. Posada-Pérez, P. J. Ramírez, R. A. Gutiérrez, D. J. Stacchiola, F. Viñes, P. Liu, F. Illas, J. A. Rodriguez, *Catal. Sci. Technol.* **2016**, 6, 6766.
- [3] K. Oshikawa, M. Nagai, S. Omi, *J. Phys. Chem. B* **2001**, 105, 9124.

- [4] X. Liu, C. Kunkel, P. Ramirez De La Piscina, N. Homs, F. Viñes, F. Illas, *ACS Catal.* **2017**, *7*, 4323.
- [5] D. Geng, X. Zhao, Z. Chen, W. Sun, W. Fu, J. Chen, W. Liu, W. Zhou, K. P. Loh, *Adv. Mater.* **2017**, *29*, 1700072.
- [6] Q. Tao, M. Dahlqvist, J. Lu, S. Kota, R. Meshkian, J. Halim, J. Palisaitis, L. Hultman, M. W. Barsoum, P. O. Å. Persson, J. Rosen, *Nat. Commun.* **2017**, *8*, 14949.
- [7] X. Zang, W. Chen, X. Zou, J. N. Hohman, L. Yang, B. Li, M. Wei, C. Zhu, J. Liang, M. Sanghadasa, J. Gu, L. Lin, *Adv. Mater.* **2018**, *30*, 1805188.
- [8] H. Bin Wu, B. Y. Xia, L. Yu, X.-Y. Yu, X. W. (David) Lou, *Nat. Commun.* **2015**, *6*, 6512.
- [9] J. Wang, W. Wang, L. Ji, S. Czioska, L. Guo, Z. Chen, *ACS Appl. Energy Mater.* **2018**, *1*, 736.
- [10] M. Chhowalla, H. S. Shin, G. Eda, L. J. Li, K. P. Loh, H. Zhang, *Nat. Chem.* **2013**, *5*, 263.
- [11] D. Voiry, A. Mohite, M. Chhowalla, *Chem. Soc. Rev.* **2015**, *44*, 2702.
- [12] Y.-C. Lin, D. O. Dumcenco, Y.-S. Huang, K. Suenaga, *Nat. Nanotechnol.* **2014**, *9*, 391.
- [13] D. Geng, X. Zhao, L. Li, P. Song, B. Tian, W. Liu, J. Chen, D. Shi, M. Lin, W. Zhou, K. P. Loh, *2D Mater.* **2017**, *4*, 011012.
- [14] Z. Liu, C. Xu, N. Kang, L. Wang, Y. Jiang, J. Du, Y. Liu, X. L. Ma, H. M. Cheng, W. Ren, *Nano Lett.* **2016**, *16*, 4243.
- [15] C. Xu, L. Wang, Z. Liu, L. Chen, J. Guo, N. Kang, X.-L. Ma, H.-M. Cheng, W. Ren, *Nat. Mater.* **2015**, *14*, 1135.
- [16] K. Leng, Z. Chen, X. Zhao, W. Tang, B. Tian, C. T. Nai, W. Zhou, K. P. Loh, *ACS Nano* **2016**, *10*, 9208.
- [17] X. Zhao, Z. Ding, J. Chen, J. Dan, S. M. Poh, W. Fu, S. J. Pennycook, W. Zhou, K. P. Loh, *ACS Nano* **2018**, *12*, 1940.
- [18] O. L. Krivanek, M. F. Chisholm, V. Nicolosi, T. J. Pennycook, G. J. Corbin, N. Dellby, M. F. Murfitt, C. S. Own, Z. S. Szilagy, M. P. Oxley, S. T. Pantelides, S. J. Pennycook, *Nature* **2010**, *464*, 571.
- [19] R. Ishikawa, E. Okunishi, H. Sawada, Y. Kondo, F. Hosokawa, E. Abe, *Nat. Mater.* **2011**, *10*, 278.
- [20] K. Yan, H. Peng, Y. Zhou, H. Li, Z. Liu, *Nano Lett.* **2011**, *11*, 1106.
- [21] W. Sun, Y. Li, B. Wang, X. Jiang, M. I. Katsnelson, P. Korzhavyi, O. Eriksson, I. Di Marco, *Nanoscale* **2016**, *8*, 15753.
- [22] X. Zhao, S. Ning, W. Fu, S. J. Pennycook, K. P. Loh, *Adv. Mater.* **2018**, *30*, 1802397.
- [23] J. S. Alden, A. W. Tsen, P. Y. Huang, R. Hovden, L. Brown, J. Park, D. A. Muller, P. L. McEuen, *Proc. Natl. Acad. Sci. USA* **2013**, *110*, 11256.
- [24] J. Chen, X. Zhao, G. Grinblat, Z. Chen, S. J. R. Tan, W. Fu, Z. Ding, I. Abdelwahab, Y. Li, D. Geng, Y. Liu, K. Leng, B. Liu, W. Liu, W. Tang, S. A. Maier, S. J. Pennycook, K. P. Loh, *Adv. Mater.* **2018**, *30*, 1704674.
- [25] J. Lin, W. Fang, W. Zhou, A. R. Lupini, J. C. Idrobo, J. Kong, S. J. Pennycook, S. T. Pantelides, *Nano Lett.* **2013**, *13*, 3262.
- [26] Y. Xie, P. R. C. Kent, *Phys. Rev. B* **2013**, *87*, 235441.
- [27] W. Sun, H. Ehteshami, P. A. Korzhavyi, *Phys. Rev. B* **2015**, *91*, 134111.
- [28] B. Hammer, J. K. Nørskov, *Nature* **1995**, *376*, 238.
- [29] B. Hammer, J. K. Nørskov, *Adv. Catal.* **2000**, *45*, 71.
- [30] D. V. Esposito, S. T. Hunt, A. L. Stottlemeyer, K. D. Dobson, B. E. McCandless, R. W. Birkmire, J. G. Chen, *Angew. Chem., Int. Ed.* **2010**, *49*, 9859.
- [31] V. Stamenkovic, B. S. Mun, K. J. J. Mayrhofer, P. N. Ross, N. M. Markovic, J. Rossmeisl, J. Greeley, J. K. Nørskov, *Angew. Chem.* **2006**, *118*, 2963.
- [32] F. H. B. Lima, J. Zhang, M. H. Shao, K. Sasaki, M. B. Vukmirovic, E. A. Ticianelli, R. R. Adzic, *J. Phys. Chem. C* **2007**, *111*, 404.
- [33] L. Gao, W. Ren, H. Xu, L. Jin, Z. Wang, T. Ma, L. P. Ma, Z. Zhang, Q. Fu, L. M. Peng, X. Bao, H. M. Cheng, *Nat. Commun.* **2012**, *3*, 669.
- [34] G. Kresse, J. Hafner, *Phys. Rev. B* **1993**, *48*, 13115.
- [35] G. Kresse, J. Hafner, *Phys. Rev. B* **1994**, *49*, 14251.
- [36] G. Kresse, J. Furthmüller, *Phys. Rev. B* **1996**, *54*, 11169.
- [37] P. E. Blöchl, *Phys. Rev. B* **1994**, *50*, 17953.
- [38] G. Kresse, D. Joubert, *Phys. Rev. B* **1999**, *59*, 1758.
- [39] J. P. Perdew, K. Burke, M. Ernzerhof, *Phys. Rev. Lett.* **1996**, *77*, 3865.
- [40] M. Methfessel, A. T. Paxton, *Phys. Rev. B* **1989**, *40*, 3616.
- [41] S. Maintz, V. L. Deringer, A. L. Tchougréeff, R. Dronskowski, *J. Comput. Chem.* **2013**, *34*, 2557.
- [42] S. Maintz, V. L. Deringer, A. L. Tchougréeff, R. Dronskowski, *J. Comput. Chem.* **2016**, *37*, 1030.
- [43] A. Togo, I. Tanaka, *Scr. Mater.* **2015**, *108*, 1.
- [44] G. Pizzi, D. Volja, B. Kozinsky, M. Fornari, N. Marzari, *Comput. Phys. Commun.* **2014**, *185*, 422.
- [45] X.-H. Zha, J. Yin, Y. Zhou, Q. Huang, K. Luo, J. Lang, J. S. Francisco, J. He, S. Du, *J. Phys. Chem. C* **2016**, *120*, 15082.
- [46] J. M. Wills, M. Alouani, P. Andersson, A. Delin, O. Eriksson, O. Grechnev, *Full-Potential Electronic Structure Method*, Springer, Berlin **2010**.